communications physics

A Nature Portfolio journal

Article

https://doi.org/10.1038/s42005-026-02518-6

Probing Earth's missing potassium using the antimatter signature of geoneutrinos

Check for updates

LiquidO Collaboration ✉*

Puzzles exist in our theories of Earth's formation and bulk chemical composition. Related to these questions is our incomplete knowledge of the planet's overall heat budget and thermal history. The successful observation of geoneutrinos originating from uranium and thorium decay chains, manifestations of the planet's natural radioactivity, serves as the only direct probe of Earth's internal, radiogenic heat engine so far. Intriguingly, potassium (^{40}K) geoneutrinos have never been observed and have so far been considered impractical to measure despite their importance in Earth's radioactive inventory. We propose here an approach for potassium geoneutrino detection that exploits their antiparticle nature. The detection framework relies on the LiquidO technique to identify positrons, thereby reducing otherwise overwhelming backgrounds. Antineutrino interactions with candidate isotope targets have been thoroughly examined and copper is found to be the ideal isotope able to meet all experimental feasibility conditions. We discuss the challenging experimental requirements to yield a potassium geoneutrino discovery.

Despite the primary constituents of the Earth being well-established and constrained[1], our inability to access the deep interior of our planet makes it impossible to measure its exact bulk composition directly. The quantification of the chemical elements present relies on compositional models, which are still under great unsettled debate. Among Earth's trace elements, there are the so-called heat-producing elements, uranium, thorium and potassium, long-lived radioactive elements whose decay has produced heat since Earth's formation.

Knowing the abundance of the Earth's heat-producing elements is fundamental to understanding the extent natural radioactivity contributes to Earth's heat flow of (47 ± 2) TW[2], wherein the remaining portion is due primarily to secular cooling. While abundances of refractory lithophile elements (U, Th) are well constrained by observations in chondrites, the silicate Earth seems strongly depleted in volatile elements, such as potassium (K). Presently, potassium is thought to contribute ~20% of the radiogenic heat produced[3]; moreover, it is believed to have played a crucial role early in Earth's formation. Indeed, because of the faster decay rate of ^{40}K ($t_{1/2} = 1.25$ Gyr), relative to ^{238}U and ^{232}Th, its contribution to the overall radiogenic heat may have reached up to ~50% in the early stages of Earth's history.

The abundance of K in the silicate Earth spans a factor of ~2 among compositional models, ranging from 130 to 280 μg/g[4]. Our planet, however, exhibits ~1/3 to ~1/8 of its predicted potassium content when compared to chondrites. The 'missing K' relative to the prediction could be due to the loss of K into space during planetary accretion[1] or segregation into the differentiating Earth's core[5]. Solving this intriguing riddle with a direct measurement would be a breakthrough in the comprehension of Earth's origin and composition, providing key tests of bulk Earth compositional paradigms and models.

The missing K problem is linked with another open question in Earth Science: the 'missing Ar'[6]. The present amount of ^{40}Ar measured in the atmosphere is approximately half of that produced within the Earth since its formation[7]. More than 99% of terrestrial argon is produced by ^{40}K decay; estimates of the bulk mass of K in the solid Earth thus determine the amount of ^{40}Ar degassed into the atmosphere. Since ratios of volatiles (e.g. H/^{40}Ar) are constant for a wide variety of rocks, the constraint on the amount of argon drives the understanding of the behaviour of other volatile elements (i.e. H, N, C and noble gases) during planetary formation and evolution, including water[8]. A fuller understanding would be possible by resolving the mysteries behind the missing fractions of K and Ar.

While powering the internal energetic processes in the Earth, beta decays of the heat-producing elements produce antineutrinos and heat, in a well-fixed ratio. A direct measurement of this antineutrino flux at the surface, ~10^6 cm^{-2} s^{-1}[9], provides an effective method for exploring Earth's inaccessible interior with unique and unrivalled insights[10,11]. In 2005, the KamLAND experiment (Japan) reported the first observation of these 'geoneutrinos'[12]. Soon after, the Borexino detector (Italy) made measurements[13,14]. Future observations are expected from SNO+ (Canada)[15] and JUNO (China)[16]. In these experiments, the detection mechanism is based on the Inverse Beta Decay reaction on free protons, here

*A list of authors and their affiliations appears at the end of the paper.
✉e-mail: anatael@in2p3.fr; mchen@queensu.ca; mantovani@fe.infn.it; andrea.serafini@pd.infn.it; strati@fe.infn.it

denoted as IBD(p). The interaction, $\bar{\nu}_e + p \rightarrow n + e^+$, provides a delayed coincidence between the e^+ and the neutron signals, correlated by a short time interval ($\tau \approx 200$ μs), and grants a distinguishing event signature with strong background rejection power. This reaction has an energy threshold of 1.806 MeV; hence only the geoneutrinos originating from the ^{238}U and ^{232}Th decay chains are detectable via the IBD(p) reaction since ^{40}K geoneutrinos have a maximum energy of 1.311 MeV (Fig. 1).

The quest to detect ^{40}K geoneutrinos requires a different reaction. Antineutrino-electron scattering is a possible reaction with no energy threshold that can be considered for ^{40}K geoneutrinos[17,18]. The drawback, though, is that this interaction produces just a single recoiling electron signal that can be easily masked by irreducible backgrounds arising from both solar neutrinos, which have a flux that is three orders of magnitude higher, and also by natural radioactivity, such as beta-minus decays or by Compton-scattered electrons produced by gamma rays. Suppression of backgrounds from radioactivity would need to greatly surpass the ultra-low background levels achieved by the Borexino experiment[19] in order to have even a hope to detect ^{40}K geoneutrinos via electron scattering.

Alternatively, instead of electrons as the target, one can consider charged-current weak interactions with atomic nuclei, as in the IBD(p) reaction, but with a target that is not hydrogen, offering a reaction with a lower energy threshold. This approach is also challenging since energy conservation establishes a minimum energy threshold of 1.022 MeV ($2m_e$) for stable isotope targets; the energy range of detectability for ^{40}K geoneutrinos is thus limited, spanning [1.022, 1.311] MeV. On the other hand, these interactions hold a special advantage owing to the fact that geoneutrinos are 'antimatter'. Indeed, the weak interaction leads to a one-to-one correlation between the production of antimatter (the geoneutrino $\bar{\nu}_e$) for every single β^- decay of matter from Earth's heat-producing elements. The antiparticle nature of geoneutrinos is evidenced by the manifestation of the positron (e^+) in the final state, like in the IBD(p) reaction; all charged-current weak interactions by electron antineutrinos produce positrons. Today's detectors cannot easily exploit this 'antimatter signature' with its potentially resilient background rejection power. With today's technology, segmented detectors have been used to identify (tag) the annihilation gamma rays produced by the e^+, as was coarsely done in the first neutrino detection[20]. Despite recent efforts[21], this remains a challenge. Identifying the e^+ unambiguously, with high efficiency, could provide the key to an experimental strategy for the detection of ^{40}K geoneutrinos.

Charged-current IBD antineutrino interactions $\bar{\nu}_e + {}_Z^AX \rightarrow e^+ + {}_{Z-1}^AY$, hereafter referred to as IBD(^{A}X), offer several possible target candidates for which the energy threshold is lower than 1.3 MeV, including those listed in ref. 22, a study that focused on radiochemical-based detection. Cadmium, not listed in ref. 22, was later proposed[23] as a promising new candidate isotope for ^{40}K geoneutrino detection. IBD(^{106}Cd) produces ^{106}Ag and an e^+. The produced ^{106}Ag subsequently decays, in turn, with an electron capture/β^+ decay branch in which an e^+ is emitted 59% of the time. ^{40}K geoneutrino capture on ^{106}Cd can thus generate two e^+ in a detector, delayed on average by the 24-minute ^{106}Ag half-life. Despite the long coincidence time, this double-e^+ signal, correlated in space and time, offers a very distinctive signature for ^{40}K geoneutrino detection.

The limitation of cadmium as a potential target is the natural abundance of ^{106}Cd. At only 1.25%, the ability to build a detector with a huge number of ^{106}Cd nuclei is unrealistic, given the anticipated size of the detector required to detect ^{40}K geoneutrinos and the prohibitive cost of isotopic enrichment, with current technology, at the required scale. Consequently, attention must be turned to other targets with high natural abundance. Moreover, for most of the possible candidates, the IBD(^{A}X) reactions do not offer a delayed coincidence signature as in the case of IBD(p) and IBD(^{106}Cd), and one must then ponder whether the clear identification of a single e^+ in a detector could be distinctive enough for

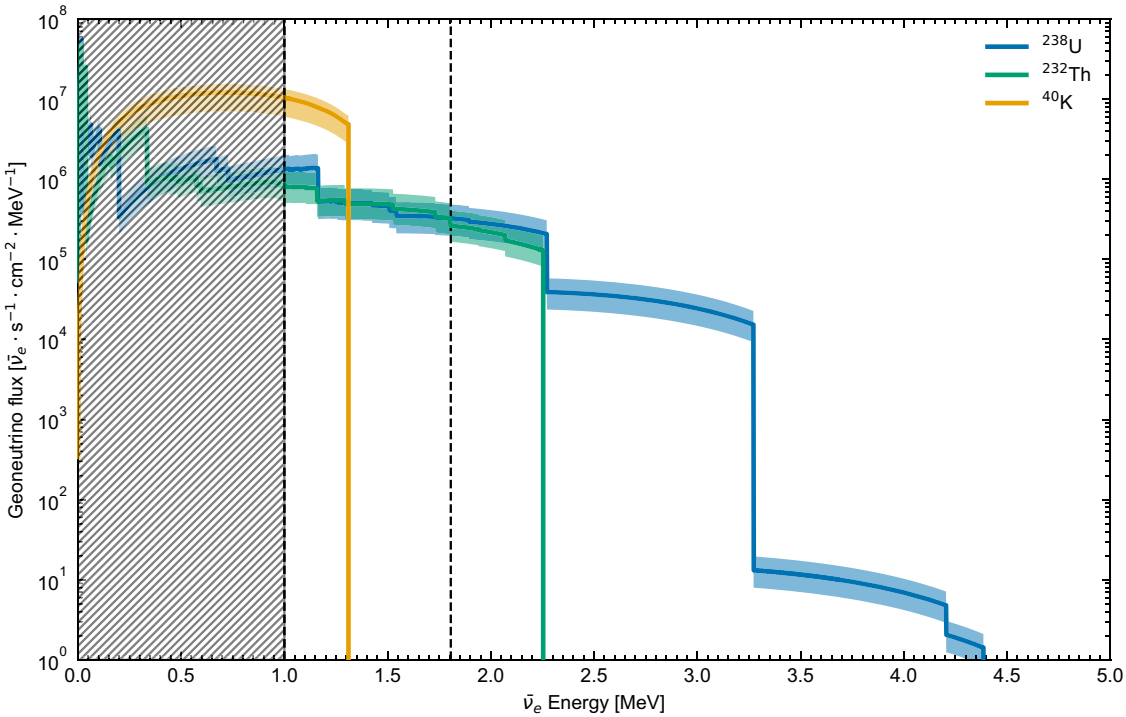

Fig. 1 | Geoneutrino energy spectra. The ^{238}U (blue), ^{232}Th (green) and ^{40}K (orange) geoneutrino fluxes expected at Laboratori Nazionali del Gran Sasso, as an example site, as a function of the antineutrino energy. The shaded lines show the variability range due to the isotopes' masses and distributions in the Earth according to the models described in the 'Methods' section, which corresponds to about ±50% uncertainty in the flux prediction. The black vertical dashed line at 1.806 MeV represents the energy threshold of the Inverse Beta Decay reaction on free protons, i.e. the reaction used by current liquid scintillator geoneutrino experiments. All contributions below the threshold are not measurable with today's technology. The region below 1.022 MeV, indicated by the black diagonal lines, represents the region which is not accessible with charged-current antineutrino capture on stable nuclear targets due to energy conservation in the reaction. The ^{238}U spectrum above 3.272 MeV has traditionally not been shown because of its very low intensity.

Table 1 | The most promising inverse beta decay (IBD) target isotopes and expected geoneutrino signals

Target process	IA [%]	E_{th} [MeV]	Log(*ft*)	Refs.	S(U) [TNU]	S(Th) [TNU]	S(K) [TNU]
$^{1}H \rightarrow {}^{1}n$	99.99	1.806	3.0170	64	31.5 [24.0, 47.0]	9.0 [6.4, 14.1]	/
$^{63}Cu \rightarrow {}^{63}Ni$	69.15	1.089	6.7	59	0.85 [0.64, 1.26]	0.49 [0.35, 0.77]	0.10 [0.07, 0.13]
$^{63}Cu \rightarrow {}^{63}Ni^{*}$		1.176	5	22			
$^{35}Cl \rightarrow {}^{35}S$	75.76	1.189	5.0088	65	0.73 [0.56, 1.09]	0.43 [0.30, 0.67]	0.10 [0.07, 0.13]
$^{106}Cd \rightarrow {}^{106}Ag$	1.25	1.212	4.1	66	(1.7 [1.3, 2.6]) × 10^{-1}	(9.7 [6.9, 15.2]) × 10^{-2}	(5.1 [3.7, 6.6]) × 10^{-3}

The 1st column lists the target and product isotopes involved in the IBD reaction, the 2nd column the IBD target Isotopic Abundance (IA) in percentage, the 3rd column the IBD reaction energy threshold (E_{th}) in MeV, the 4th column the Log(ft) value for the corresponding β decay of the final state, which is a measure of the reaction cross section. The IA, E_{th} and Log(ft) values are taken from the ENSDF database[59], whose specific references are found in the 5th column. The 6th, 7th and 8th columns report, as central values, the expected geoneutrino signal in the [E_{th}, 3.272] MeV energy range respectively from uranium, thorium and potassium distributed in the Earth's lithosphere and mantle. The hypothetical location of the Laboratori Nazionali del Gran Sasso has been chosen as example site. The range in square brackets provides the variability of the expected predicted signal, thus defining the 'minimal' and 'maximal' scenarios for the masses and distributions of heat-producing elements in the Earth determined with different Bulk Silicate Earth compositional models. See 'Methods' for further details. The expected geoneutrino signals are given in Terrestrial Neutrino Units (TNUs), corresponding to a 1-year acquisition time and 10^{32} atoms for each chemical species (i.e. a number of IBD target atoms corresponding to 10^{32} scaled by the isotopic abundance) and assuming 100% efficiency. Chlorine (^{35}Cl) and copper (^{63}Cu) represent the most promising targets for ^{40}K geoneutrinos detection, while hydrogen (^{1}H), and cadmium (^{106}Cd) are here reported for comparison. A full list of the suitable target isotopes for ^{40}K geoneutrinos detection can be found in the 'Methods' section.

robust detection of ^{40}K geoneutrinos. Could the 'antimatter signature' of geoneutrinos be reliably exploited for efficient detection and background control?

The scientific and technological development foreseen for detecting these low-energy antineutrinos, together with their relevance in Earth Science, make the ^{40}K geoneutrino measurement the 'holy grail' for neutrino geoscientists. For exploring this low energy region of the geoneutrino spectrum (Fig. 1), considered today as being practically impossible, a complete (to the best of our knowledge) set of reactions, meeting all the necessary conditions, such as energy threshold (<1.3 MeV), natural abundance, and cross section, are discussed in this article, together with a possible experimental detection technique which features the unambiguous identification of single e^+ signals in a detector that greatly suppresses today's most limiting backgrounds. In our study, we identified a single suitable isotope—^{3}Cu appears to be the ideal candidate for ^{40}K geoneutrino detection.

Results and discussion

The LiquidO technique[24] enables the clear identification of e^+ in a scintillation detector arising from both the spatial topology of the event and the time pattern for energy deposition and light collection. The unique double-e^+ signal of the ^{106}Cd geoneutrino reaction, combined with the ability of LiquidO to unambiguously detect positrons, initially prompted this study of ^{40}K geoneutrinos. Later, we focused solely on exploiting the positron's "antimatter signature" as the essential fact. We therefore examined several potential candidate interactions that lead to a single-e^+ manifestation to enable the detection of ^{40}K geoneutrinos. The identification of a positron annihilation signal in a detector, in and of itself, strongly suppresses other backgrounds (e.g. from natural radioactivity). Though there are potential background sources that can produce true e^+ (or β^+) signals in a detector, discussed in detail later in this article, they are much rarer than those that produce single electrons (or β^-). LiquidO's approach provides both a distinct e^+ event signature as well as the means for deploying promising targets for ^{40}K geoneutrino detection via high-level detector doping, thanks to its opacity-based detection medium.

Candidate targets for ^{40}K geoneutrino detection

Table 1 lists the most promising target isotopes for IBD(^{A}X) with low enough threshold and high natural isotopic abundance. The estimated signal event rates are provided, including those of IBD(*p*) and IBD(^{106}Cd) for comparison. Since crustal thickness and concentration of heat-producing elements varies with global location, the intensity of geoneutrino signals is strongly dependent on the detector site. In the following calculations, the Laboratori Nazionali del Gran Sasso (Italy) was chosen as an example site, given its average crustal thickness (35 km) being an intermediate case between the extreme value of thin oceanic crust (e.g. Hawaii, 5 km) and the thickest continental crust (e.g. Himalayas, 70 km). Full details of the cross-section estimates, rate calculations and a longer list of potentially suitable target isotopes for ^{40}K geoneutrinos detection can be found in the 'Methods' section and Supplementary Table 3, including arguments for why others were discarded.

Figure 2 shows the cross section and detected energy spectrum for several proposed targets, revealing that the most promising isotopes for detecting ^{40}K geoneutrinos are ^{35}Cl and ^{63}Cu, after weighting the event rates by their isotopic abundance. The ^{40}K geoneutrino signal rates are roughly the same for chlorine and copper, and area factor of ~20 higher than the signal rate in the next best choice (cadmium), diminished by its poor natural abundance. Both Cl and Cu have then been further evaluated in our study as to their susceptibility to potential backgrounds and the ability to deploy either of them in a detector. The detection technique being proposed here is potentially suitable for doping with either Cl and Cu, and will be described next before specific evaluation of Cl and Cu in a hypothetical LiquidO detector.

LiquidO

The LiquidO detection technique has two features that make it ideal for the detection of ^{40}K geoneutrinos. The first is that the requirement of very high transparency for the liquid scintillator is relaxed in LiquidO because scintillation light gets collected using an array of closely spaced wavelength-shifting fibres distributed throughout the detector. Organic liquid scintillators can be doped with various elements[25]; traditionally, this has potentially affected the transparency and intrinsic light yield of the resultant liquid scintillator cocktail. LiquidO's tolerance to reduced transparency opens up the possibility to dope detectors with many elements to higher loading fractions and is well aligned with the main objective here—finding the best isotope candidates to be used as targets for charged-current reactions with low energy thresholds.

The second feature of LiquidO applicable to geoneutrino detection is its powerful particle identification capability owing to stochastic confinement of light[26]. In a medium with a short mean-free path for light scattering (mm or less), scintillation light is stochastically confined near the energy deposition loci where it's produced, until collected by a grid of wavelength-shifting optical fibres. Reading out the light (proportional to the energy deposited) collected by the fibres produces an image of the topology of the energy deposited, with the time pattern for the light to be collected also providing information. This is referred to as energy flow in LiquidO (Fig. 3b, c). Positron event topology can be imaged in LiquidO (Fig. 3a), in which the e^+ central kinetic energy deposition and its two annihilation gamma rays are readily identified. Indeed, LiquidO's ability to unravel the positron annihilation pattern is so striking that the technique is currently being explored for high performance positron imaging[27]. This capability makes LiquidO well-suited to detect antineutrinos; this distinctive e^+ signature tag can be exploited for IBD(^{35}Cl) and IBD(^{63}Cu) observation, perhaps even without the need for a delayed coincidence.

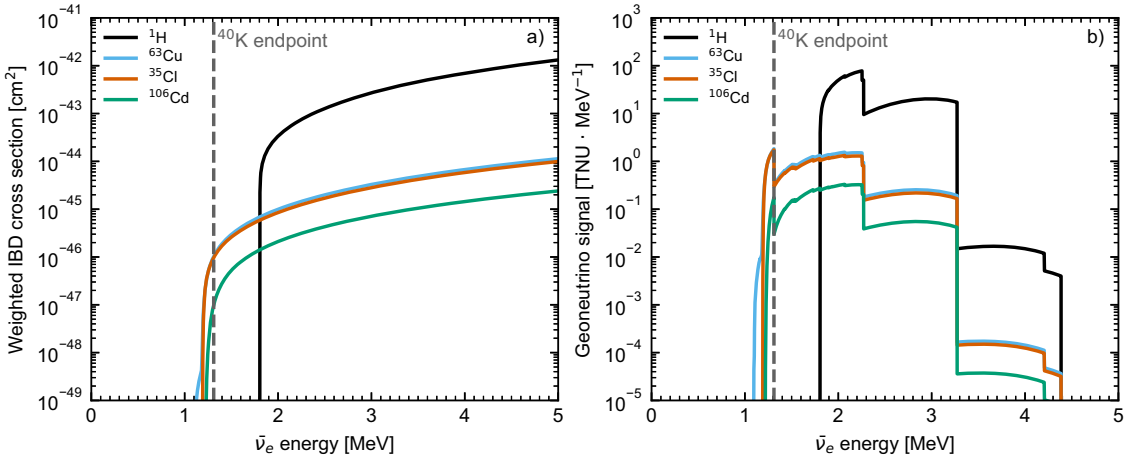

Fig. 2 | Cross sections and expected geoneutrino measured spectra for the ^{1}H, ^{35}Cl, ^{63}Cu and ^{106}Cd inverse beta decay (IBD) targets. a shows IBD reaction cross sections for the 4 different targets as a function of the incoming antineutrino energy, weighted by the corresponding target isotopic abundance (see Table 1). **b** shows the expected geoneutrino measured spectra at the Laboratori Nazionali del Gran Sasso (Italy), as an example site, originating from uranium, thorium and potassium distributed in the Earth's lithosphere and mantle, calculated as described in the 'Methods' section. The expected geoneutrino spectra are given in Terrestrial Neutrino Units (TNUs). In both figures, the dashed vertical line indicates the endpoint of the potassium geoneutrino spectrum at 1.311 MeV.

Extracting the ^{40}K geoneutrino signal

It is instructive to first consider the detection of ^{40}K geoneutrinos using a LiquidO-style detector, using IBD(^{35}Cl). Chlorine can be easily loaded in an organic liquid scintillator, and there are several possible ways to achieve high doping, up to a hypothetical 50% in weight. For instance, a chlorinated-benzene compound could be used as a liquid scintillator in LiquidO. Several compounds, such as (but not limited to) dichlorobenzene ($C_6H_4Cl_2$), fluoresce and can function as (or together with) a liquid scintillator. Moreover, chlorine could also be doped in a typical liquid scintillator by mixing in a non-fluorescing chlorinated solvent such as tetrachloroethylene (C_2Cl_4). These are only given as examples and are not being proposed for implementation; dedicated R&D will be required to fully develop feasible loading approaches.

Table 1 shows that the rate of IBD(p) events from U and Th geoneutrinos is much larger than IBD(^{35}Cl) from ^{40}K geoneutrinos. A chlorine-loaded detector that has abundant hydrogen, as in most liquid scintillators, will also record many IBD(p) reactions, serving to measure U and Th events with high statistics. One thus measures the U and Th geoneutrino fluxes using the IBD(p) events, tagged by their neutron capture, to allow their contribution to the IBD(^{35}Cl) events to be extracted and inferred, as illustrated in Fig. 4.

In evaluating the concept of single e^+ identification in LiquidO with chlorine, the central question remains: without a delayed coincidence, would a single e^+ be a robust enough signal compared to backgrounds? Even if e^+ events can be easily distinguished from normal α, β and γ radioactive backgrounds, are there any backgrounds that produce actual e^+ events in a detector, and how do these background rates compare to the anticipated ^{40}K geoneutrino signal's very low rate?

Backgrounds

There are indeed genuine positron backgrounds. They come from other antineutrinos (from nuclear power reactors and U/Th geoneutrinos) and from β^+ emitting background sources. The latter are considerably rarer than β^- backgrounds, which helps make the problem somewhat tractable. Finally, there are gamma-ray interactions that can produce or mimic the e^+ signature. Table 2 summarises the nature of all backgrounds and how they might be dealt with and suppressed in a LiquidO detector.

The antineutrino backgrounds, though irreducible, are easily managed. Using IBD(p) reactions in the liquid scintillator, reactor antineutrinos and U and Th geoneutrinos can be well measured and constrained in the same detector with minimal or no reliance on predictions. Within the narrow energy range, above the IBD(^{A}X) reaction threshold and below the endpoint (1.3 MeV), ^{40}K geoneutrinos substantially dominate, and the contributions even from a relatively large reactor antineutrino flux will be insignificant (excluding sites that are extremely close to nuclear reactors). Figure 4 illustrates the method for the quantification and statistical subtraction of this irreducible background. The excess of e^+ events in the proper energy range, above the predicted background from U, Th geoneutrinos and reactor antineutrinos, is expected to be a clean sample of ^{40}K geoneutrinos.

A minor contribution comes from the neutrinos and antineutrinos produced in pionic and muonic decays in the atmosphere, typically referred to as atmospheric neutrinos, which can interact with the nuclei constituting the scintillator and the doping isotopes. Given that the signal is a low-energy single positron, the main contribution from atmospheric neutrinos is expected to be mainly from electron-flavour antineutrinos undergoing the IBD(^{A}X) reactions. In this context, only neutrinos whose energy is very close to the reaction energy threshold would be important. Interactions on carbon have also been considered. Given the tight signal topology, narrow energy acceptance constraints, and the fact that the atmospheric neutrino flux falls steeply with energy[28], this background is determined to be negligible. The estimates from running experiments without topological e^+ tagging, such as Borexino, SNO+ and KamLAND[29], confirm a negligible predicted impact.

Of greater concern are β^+ decaying backgrounds. In natural radioactivity, there is perhaps only one important β^+ emitter, that being ^{40}K itself. Low-background physics experiments have learned how to reduce this background to very low levels, with the primary concern typically being the 1.46 MeV gamma ray that is emitted following the electron capture decay branch 10.67% of the time. In comparison, the β^+ decay branching ratio is 10^{-5}. With the remarkably low levels of ^{40}K achievable in a liquid scintillator[19], one can estimate this background to be less than one such β^+ decay per 100 kilotons of detector per year. The energy spectrum of the e^+ background from ^{40}K in the detector extends to higher energies than the e^+ signals produced by ^{40}K geoneutrino charged-current interactions on ^{35}Cl or ^{63}Cu. This provides another handle for discriminating this background, as less than 15% of the energy spectrum of the e^+ produced by ^{40}K-β^+ decays overlaps with the ^{40}K geoneutrino spectrum. The trace amount of ^{40}K in the scintillator can also be precisely estimated through the observation of the much more common 1.46 MeV gamma-ray emission and then used to derive its abundance in situ, in order to subtract its expected e^+ background in the ^{40}K geoneutrino energy region.

Another possible source of β^+ emitters are isotopes produced by cosmic-ray interactions with materials in the detector[30], especially while

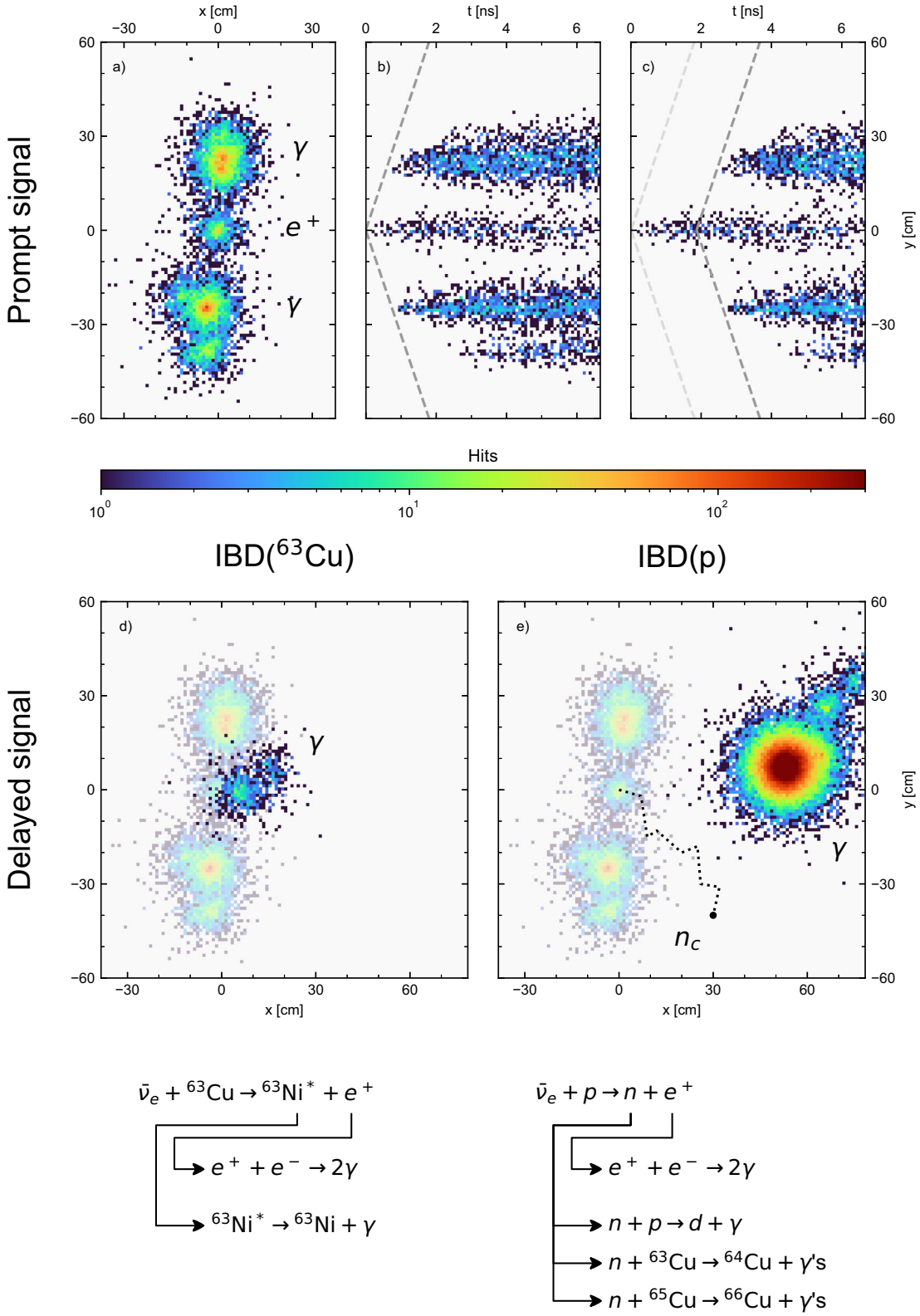

those materials are on the surface. Short-lived isotopes that are produced can, in principle, be vetoed by identifying the cosmic-ray muon passing through the detector and applying a position-time veto window in which subsequent events are rejected. Tracking muons with high precision will be possible with LiquidO and is expected to be very effective. However, long-lived isotopes are also a possibility and, if an excessive amount were produced at the surface, it would require an extreme purification campaign, almost necessarily to be conducted underground, to remove the activated cosmogenic isotopes, if possible. Cosmogenic β^+ emitters can represent a major concern for the detection of ^{40}K geoneutrinos and we will return to this topic.

To complete the discussion of e^+ backgrounds, one must consider gamma rays and how they might mimic the sought-after e^+ signature. Gamma rays can produce true e^+ in a detector through pair production.

Fig. 3 | Simulated inverse beta decay (IBD) events in a LiquidO detector doped with copper. a shows the event topology of a 100-keV single e^+ featured by its emission of two back-to-back 511-keV annihilation gammas to be used for event-wise tagging. This topology is common to IBD(*p*) and IBD(^{63}Cu) events upon the e^+ emission. **b** shows the time pattern for the scintillation light (energy) to be collected in LiquidO for the e^+ event shown in (**a**), assuming that the annihilation of the e^+ is immediate, as opposed to the formation of ortho-positronium, depicted in (**c**), that typically delays the annihilation by a few ns. The topology and the time pattern of a positron annihilation are the key signatures for any IBD interactions, and they will be key tagging features for IBD(^{63}Cu). The energy flow (i.e. the topology of the energy deposition as a function of time) reveals the two annihilation gamma rays propagating away from the point of the e^+ energy deposition. The scintillation light produced by subsequent multiple gamma ray Compton scattering diffuses with a speed lower than the speed of light (represented by the grey dashed lines) and is collected by nearby fibres and sums to 511 keV of energy deposited by each gamma ray. **d** shows the event topology of the delayed 87 keV gamma ray from the de-excitation of ^{63}Ni* following a prompt e^+ signal of an IBD(^{63}Cu) reaction. Last, **e** shows the event topology of the delayed gamma ray produced in the neutron capture on hydrogen following a prompt e^+ signal of an IBD(*p*) reaction. The neutron that emerges from the point of interaction in (**d**) captured at the point labelled n_c. Neutron captures on copper would also be easily identified in LiquidO because numerous gamma rays are emitted with a large total energy, with reaction *Q*-values of 7.9 MeV and 7.1 MeV for ^{63}Cu and ^{65}Cu, respectively. The presence of Cu also shortens the time coincidence between prompt (e^+) and the delayed neutron capture, allowing better accidental background reduction. The e^+ annihilation is shown faded in (**c**, **d**), representing the fact that it occurred prior to the depicted delayed signals. The LiquidO vertex position precision is expected to be at the sub-cm level, up to ~1 mm depending on the detector readout configuration, further improving accidental coincidence and cosmogenic background rejection via the correlation with a preceding cosmic muon track. All the plots have a common colour-coded *z*-scale indicating the raw number of photons hitting the LiquidO fibres, labelled 'hits'. The simulated fibre spacing is 1 cm in these plots. The photon detection efficiency has not been included as it is specific to the detector configuration and optimisation studies are in progress.

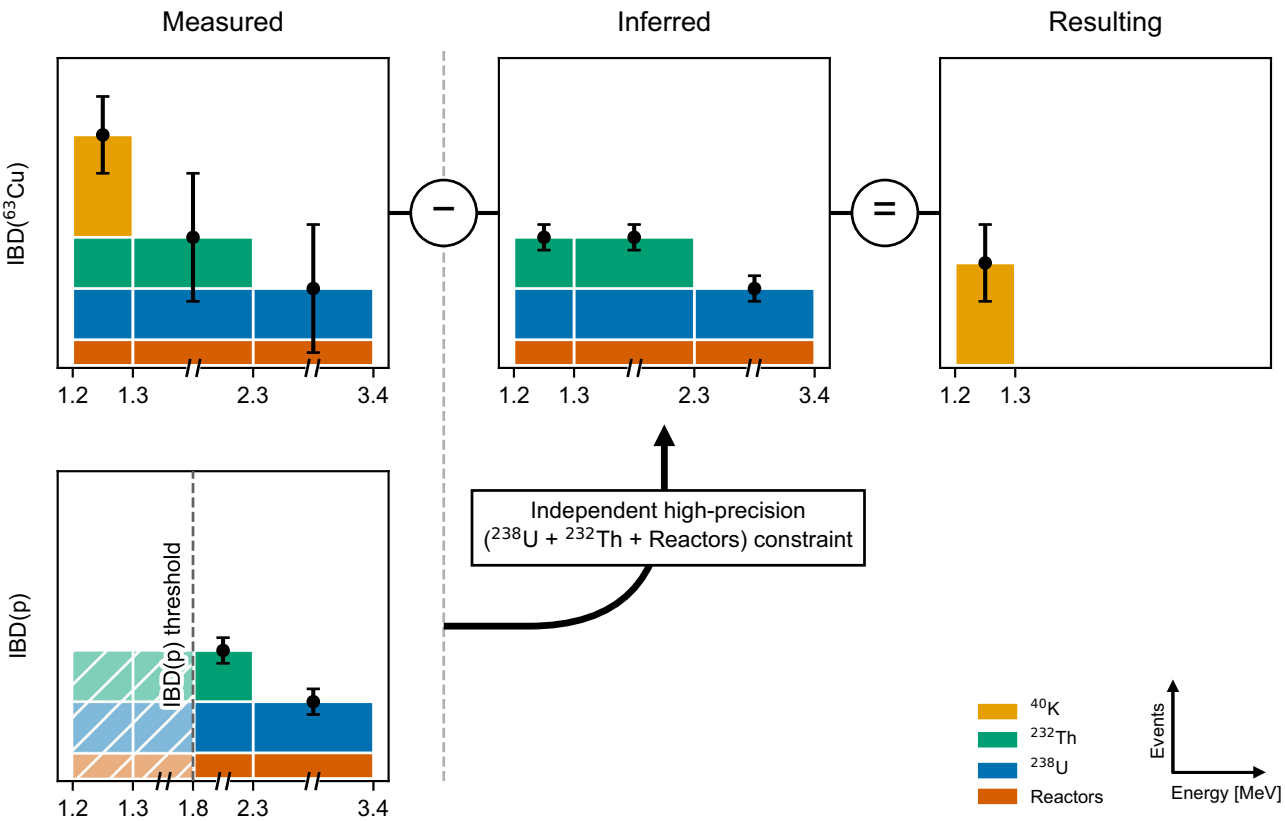

Fig. 4 | Methodology for ^{40}K geoneutrino signal extraction. Reactor antineutrinos as well as ^{238}U and ^{232}Th geoneutrino fluxes are determined with small uncertainty by high-statistics measurements of Inverse Beta Decay or IBD(*p*) events from which their contribution to IBD(^{63}Cu) events can be inferred at the percent-level. Those same antineutrino contributions need to be subtracted over the [1.189, 1.311] MeV geoneutrino energy range, as they are effectively an irreducible background to the IBD(^{63}Cu) based ^{40}K geoneutrino signal. The histograms are illustrative; their amplitudes are not to scale, and the error bars qualitatively represent the expected statistical uncertainty for each component, highlighting the contrast between the well-measured IBD(*p*) signal components and the low-statistics IBD(^{63}Cu) signal.

The subsequent annihilation of the e^+ produces the expected event topology in LiquidO. The ^{40}K geoneutrinos produce e^+ with very little kinetic energy, between [0, 0.289] MeV. The pair production cross section on Cu and Cl is ~10^{-3} times that of Compton scattering at these energy[31]. With pair production suppressed, it seems feasible that energy information of the candidate e^+ event, together with requiring no previous interaction of the gamma ray prior to it undergoing pair production, could be sufficient to reject this background. The specific quantification of this background requires detailed simulations for different doping scenarios that consider the radiation properties of the medium (a subject of future feasibility studies).

The final background that was considered is from multiple Compton scatterings of gamma rays that could, by chance, mimic the e^+ signature. The energy flow information that is accessible in an event in LiquidO would strongly suppress this background. A true e^+ event originates the two 511 keV annihilation gamma rays from the same point, propagating with the speed of light. Multiple Compton scatters would tend not to produce these two simultaneous and displaced energy depositions with the topology and resolution granted by LiquidO, as illustrated in Fig. 3. Furthermore, the antineutrino-produced positron can also lead non-negligibly to the formation of positronium – an unstable exotic atom with a loosely-bound electron[32]. Both the formation and stability of positronium depend on the

Table 2 | Backgrounds to the ^{40}K geoneutrino e$^+$ signal in LiquidO

e$^+$ backgrounds		
Source	**Expectation**	**Suppression**
IBD(^{A}X) of U and Th geoneutrinos	~1/5 rate of predicted ^{40}K geoneutrinos in K energy interval	Irreducible but measured by IBD(*p*)
IBD(^{A}X) of reactor antineutrinos	~1/60 rate of predicted ^{40}K geoneutrinos in K energy interval	Irreducible but measured by IBD(*p*)
β$^+$ decays of naturally occurring ^{40}K in the detector	~10^{-5} e$^+$ per year per ton	Use of decay energy spectrum to constrain
β$^+$ decays of cosmogenic isotopes	Similar to β$^+$ isotope production in current experiments	Cosmic muon veto and energy spectrum for further suppression
Pair production (e$^+$-e$^-$) by gamma rays (conversion)	Pair production cross section in the [1.022, 1.144] MeV range is ~10^{-3} times the Compton scattering cross section that dominates in current experiments	Gamma rays make other interactions prior to converting; LiquidO event pattern helps reject
Multiple Compton scattering (fake e$^+$ signal)	e$^+$ signal is still very distinctive compared to gamma-ray-induced single electron recoils	Monte Carlo study of rejection of gamma rays using event pattern and energy flow

The ^{40}K geoneutrino signal is a single e$^+$ that can be identified in LiquidO, as illustrated and described in Fig. 3. All possible backgrounds, including irreducible antineutrinos, true e$^+$ sources and gamma rays converting or faking e$^+$ events, are listed in the table, along with a brief note on how these backgrounds compare and how they might be further suppressed. Further details can be found in the main text.

type of medium[33], including the possible presence of doping[34]. This leads to possible variations in the formation rate and annihilation pattern exhibited mainly due to the production of ortho-positronium[32] with differences in lifetime and number (i.e. two or three) of annihilation gammas. In traditional scintillators, the ortho-positronium formation fraction can be as high as ~50%, with a decay time of order ≤3 ns[33], consistent with previous, precise observations in antineutrino experiments[35]. The rich positronium pattern may provide an extra handle for background control in a LiquidO-based detector (Fig. 3) and can be experimentally characterised with good precision for a given scintillator configuration[33,34].

We conclude this discussion of e$^+$ backgrounds by postulating that a future experiment might be able to control gamma-ray backgrounds sufficiently well, with the signature of e$^+$ annihilation then being sufficiently distinctive. The feasibility of this approach depends heavily on LiquidO's detection and doping performance, still under experimental validation. The potential to detect ^{40}K geoneutrinos with LiquidO appears a priori feasible.

This brings us to a final discussion of possible backgrounds specific to the two elements identified for detecting ^{40}K geoneutrinos: copper and chlorine. For the case of chlorine as a geoneutrino target, despite having one of the highest cross sections among the possible targets and the ability to dope chlorine in a liquid scintillator being known, there is a problematic cosmogenic background. Natural chlorine contains trace amounts of the radioisotope ^{36}Cl, at the part in 10^{13} level. This isotope is produced in the atmosphere by spallation, by cosmic-ray interactions on ^{36}Ar, and in the upper part of the lithosphere by thermal neutron activation of ^{35}Cl. With a half-life of 3×10^5 years, and a β$^+$ decay branch with 0.02% probability, this isotope would produce ~10^{10} positrons per year per 10^{32} chlorine atoms. This would completely overwhelm the ^{40}K geoneutrino expected event rate (~0.1 TNU; the Terrestrial Neutrino Unit is equal to the number of geoneutrino interactions per year per 10^{32} target atoms). Chemical purification does not separate chlorine isotopes and large-scale isotopic separation is unfeasible. For this reason, using chlorine to search for ^{40}K geoneutrino interactions must be ruled out. The authors have highlighted this otherwise promising candidate to note the importance of carefully considering cosmogenic production of trace isotopes in rare event searches. The low event rate and possible impact of unknown combinatory backgrounds strongly favour identifying another candidate target element with a more robust signal topology, if possible, and not suffering from having a long-lived cosmogenic β$^+$ emitter.

Copper—an ideal candidate

Copper is a candidate for doping in LiquidO for ^{40}K geoneutrino detection, with an expected event rate as high as that for chlorine. Doping copper in an organic liquid scintillator has not been previously accomplished. Nevertheless, techniques exist for producing scintillator cocktails that are miscible with water. Copper in aqueous solution could thus be loaded. Organocopper compounds also exist, and the chemistry of copper is arguably more varied than that of chlorine. The LiquidO approach that employs an opaque scintillator, with a short light-scattering length, is amenable to new metal-loading approaches (e.g. dispersion of nanoparticles). At 69% natural isotopic abundance, ^{63}Cu would be the specific isotope that has a low enough energy threshold for IBD(^{63}Cu) to be usable to detect ^{40}K geoneutrinos.

The ground state of ^{63}Cu has spin-parity 3/2$^-$. IBD(^{63}Cu) reactions would lead to the ^{63}Ni ground state (1/2$^-$) or ^{63}Ni* excited state (5/2$^-$) at the 87 keV energy level; both allowed transitions, with favourable cross sections. The cross section for the transition to the ^{63}Ni ground state can be estimated from ^{63}Ni β decay using its Log(*ft*) value, branching ratio and decay spectrum. On the other hand, for transitions to the ^{63}Ni* excited state, there are no previous measurements of the β decay partial half-life for this nuclear state. We have assumed a typical Log(*ft*) value of 5, as was done in ref. 22, noting that the Log(*ft*) value to the ^{63}Ni ground state transition is worse (Log(*ft*) = 6.7). The ^{63}Ni* excited state has a higher *Q*-value and thus its associated β decay half-life should be shorter, leading to a smaller Log(*ft*) value and a higher cross section. One would need to confirm or measure the IBD(^{63}Cu) cross section to the excited state using either a new measurement of ^{63}Ni* β decay—unlikely to be realised for practical reasons—or invoke arguments from nuclear theory for this cross section based on experimental results from ^{63}Cu(*n*, *p*) nuclear reactions.

IBD(^{63}Cu) transitions to ^{63}Ni* have another advantage. The excited state has a lifetime of 1.67 μs for decaying by emission of a gamma ray with 87 keV energy. This would provide a delayed coincidence that is exploitable to reject backgrounds, including true e$^+$ backgrounds. Explicitly, IBD(^{63}Cu → ^{63}Ni*) would first produce an identified e$^+$ signal in a LiquidO detector, followed by the detection of an 87 keV gamma ray correlated in time and space with the e$^+$, illustrated in Fig. 3d. With a high Cu loading fraction, photoelectric absorption (dependent on atomic number) of the low energy gamma ray would be most probable, and the expected signal would be a single-point energy deposition of 87 keV. The specific energy and the isolated event topology, near the IBD(Cu) e$^+$, would make this delayed event extremely distinctive, leading to an overall major improvement in the robustness of the method.

For cosmogenic backgrounds, copper also has advantages compared to chlorine. Copper does not have long-lived β$^+$ decaying isotopes. ^{64}Cu ($t_{1/2}$ = 12.7 h) is relatively short-lived; it can be produced by neutron activation, and it decays with both β$^-$ and β$^+$ emission, with a branching ratio of 17.6% for β$^+$ decay. Reducing neutron exposure would be important and might imply overburden constraints for the detector that are not expected to be onerous.

Potential sources of neutrons in a detector are: (i) cosmic-ray neutrons impinging on the detector, (ii) muon-induced neutrons generated by electromagnetic/hadronic interactions of fast muons or by muon capture on nuclei in or surrounding the detector (iii) neutrons created by (*α*, *n*)

Table 3 | Expected number of geoneutrino and reactor antineutrino events

Detection reaction	Energy range	Events/10 yr/240 ktons			
		Reactors	^{238}U	^{232}Th	^{40}K
IBD(p)	[1.806–3.27] MeV	19530	27750	7948	/
IBD(^{63}Cu → ^{63}Ni*)	[1.176–1.311] MeV	0.2	1.1	1.1	11.7

Antineutrino events estimated using a LiquidO detector located at the Laboratori Nazionali del Gran Sasso (Italy), as an example, and having a mass of 240 kton with 50% Cu loading and considering 10 years of data taking. Full details regarding the calculation of the geoneutrino and reactor antineutrino event rates are described in the 'Methods' section.

reactions and those following the spontaneous fission of U in the rocks around the detector's experimental hall and (iv) neutrons produced as a result of the IBD(p) process itself. Cosmic ray-induced neutrons do not represent a major concern; the flux would be completely attenuated by placing the detector below the Earth's surface. The only concern would be exposure of the liquid scintillator to the surface neutron flux before detector filling. As the half-life of ^{64}Cu is short, after activation at the surface, the copper would only need to "cool" for a period of several days (~11 days would provide a factor >10^6 reduction). The underground copper-loaded detector would still need to be surrounded by thermal neutron shielding to minimise continuous activation of ^{64}Cu. Passive or active shielding (e.g. a water pool) would also prove effective in reducing the flux of neutrons produced by muons interacting with the rocks surrounding the detector. Cosmic-ray muons and muon-induced neutrons may produce some ^{64}Cu nuclei; however, muons are efficiently tagged in neutrino detectors, especially in LiquidO, where active vetoing techniques can be employed to further suppress ^{64}Cu backgrounds via temporal and spatial fiducial cuts around a muon track. Even for a detector that is well shielded and underground, cosmic-ray muons might not be completely suppressed and would generate some equilibrium level of ^{64}Cu in a detector. A future experiment would need to be designed to efficiently tag muon-induced neutrons that might activate ^{64}Cu at a trace level.

The last source of neutrons to consider originates from the IBD(p) reaction itself. These reactions produce a neutron in the scintillator. This neutron is critical for the identification of IBD(p) reactions. Any misidentification could lead to confusion between the IBD(p) and IBD(^{63}Cu) detection channels, making it effectively impossible to detect IBD(^{63}Cu) events, which are statistically disfavoured by several orders of magnitude, as shown in Table 3. Both of the naturally occurring copper isotopes, ^{63}Cu and ^{65}Cu, have neutron capture probabilities much higher than hydrogen[36,37], with ^{63}Cu having the highest cross section[38]. Neutron captures on copper are easily identified in LiquidO because of the numerous gamma rays emitted in the process, with a large total energy (i.e. reaction Q-value) of 7.9 MeV and 7.1 MeV for ^{63}Cu and ^{65}Cu, respectively[38]. In this case, the produced ^{64}Cu β^+ emitter can be spatially and temporally vetoed on the basis of the detected gamma rays following the ^{63}Cu neutron capture. To recapitulate, if an IBD(p) event produces a neutron that is captured, for example, on ^{63}Cu, the IBD(p) is not missed because of the distinctive neutron-capture gamma signal. If the produced ^{64}Cu later undergoes β^+ decay, this can be associated with the previous IBD(p) event's neutron-capture position, and thus, this e^+ is not counted as a background event for the IBD(Cu) signal.

Detection significance estimation

To estimate the ^{40}K geoneutrino detection significance in a future experiment, consider the Poisson probability distribution of the hypothetical observation of N or greater events compared to the null hypothesis that the experimental observation came from only backgrounds:

$$\sum_{n=N}^{\infty} P\left(n;\mu+\Delta\mu\right) \tag{1}$$

where N is the number of observed events, μ is the mean expected number of background events in the null hypothesis, and the uncertainty of the total background $\Delta\mu$ (both statistical and systematic contributions) can be accounted for by adding it to the mean[39]. A more formal likelihood calculation yields similar results because of the small rates and uncertainties involved. Generally, if the expected background is uncertain but can be constrained by a separate measurement, the background as a nuisance parameter in the likelihood function for a Poisson counting experiment can also be well constrained. It essentially reduces the significance calculation to counting statistics of the anticipated signal versus possible fluctuations of the known background.

We consider the case of copper with an identified 87 keV γ in delayed coincidence. Backgrounds such as pair production or fake e^+ signals from multiple Compton scattering are eliminated by time-position-energy coincidence requirements. As argued above, we will assume that natural and cosmogenic radioactivity of β^+ emitters can also be suppressed, measured and constrained, and ultimately also eliminated by the coincidence requirement.

Only the irreducible antineutrino backgrounds remain to be quantified, in comparison to the ^{40}K geoneutrino signal. In this case, the separate measurement of the U and Th geoneutrino background in the ^{40}K geoneutrino energy range comes from the IBD(p) events, previously discussed. Due to the relatively high rate of IBD(p) events in a hydrogen-rich liquid scintillator, the fractional uncertainty of this background contribution will be small. One of the keys here that yields maximal discovery sensitivity is the data-driven subtraction of the U + Th signal, whose accuracy cannot be achieved via predictions based on geological arguments alone.

The statistical and systematic uncertainties in the reactor background contribution in the ^{40}K geoneutrino energy range must also be included. Sites with minimal reactor contributions are certainly favoured; but even if the flux is relatively high and even if their uncertainties are fractionally much larger, they will still have minimal impact since the absolute event rate from reactor events in the proper energy range is so much smaller, as shown in Table 3.

All systematic uncertainties (U, Th and reactors) can be included in the $\Delta\mu$ term, in the calculation of the Poissonian probabilities. The fact that U + Th geoneutrino backgrounds to the IBD(^{63}Cu) events are directly measured by IBD(p) events in the same detector helps, as many systematics related to their relative rates cancel, enhancing the robustness of the proposed experimental methodology. There are some systematics that would need to be considered that affect the low-energy (≤1.8 MeV) IBD(^{63}Cu) signal differently than the higher-energy IBD(p) signal, such as reaction cross section uncertainties; U, Th and reactor spectrum shape uncertainties at those energies; and energy-dependent detector systematics. Most of these could be experimentally explored by taking ancillary data close to a reactor with a small detector, also measuring the ^{63}Cu antineutrino capture cross section to the excited state ^{63}Ni*. Ultimately, systematic uncertainties in the background estimations wind up having little impact on the ^{40}K geoneutrino flux measurement (and its significance) since the ^{40}K geoneutrino signal is nearly an order of magnitude larger than each of the U and Th geoneutrino backgrounds, as quantified in Table 3. The resulting ^{40}K geoneutrino detection significance as a function of the detector mass is plotted in Fig. 5, together with the attainable flux measurement precision for U and Th geoneutrinos.

The methodology for extracting the ^{40}K geoneutrino signal (Fig. 4) requires extrapolating the U and Th geoneutrino components plus the reactor backgrounds into the ^{40}K geoneutrino energy window. The presence of two classes of events, IBD(^{63}Cu) and IBD(p), makes efficient neutron tagging a strict requirement. Any IBD(p) event that fails to reconstruct the accompanying neutron could be misidentified as an IBD(^{63}Cu) event (or as a background e^+ event) that is missing the delayed 87 keV gamma ray from true IBD(^{63}Cu → ^{63}Ni*), with the potential that those at low kinetic energies are mistaken for ^{40}K geoneutrinos. LiquidO with copper is expected to have an enhanced neutron tagging efficiency since thermal neutron capture on copper is rather characteristic, as previously discussed.

To summarise, IBD(p) events produce an e^+ signal and a neutron. The neutron must be efficiently identified so that IBD(p) events accurately

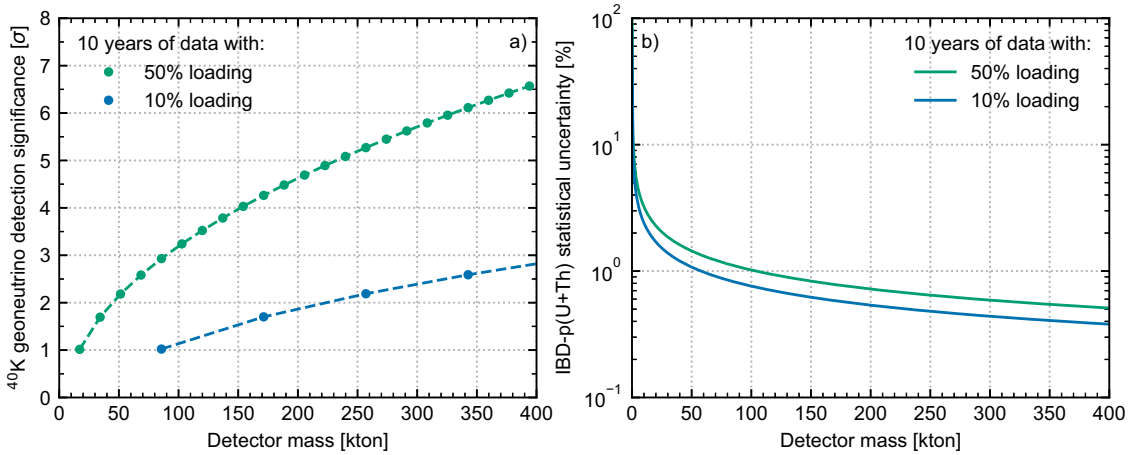

Fig. 5 | ^{40}K geoneutrino detection significance and statistical uncertainty on U + Th signal. a, b refer to a Cu-loaded detector running for 10 years at the Laboratori Nazionali del Gran Sasso, as an example. The expected geoneutrino signal and the irreducible reactor and geoneutrino backgrounds in the Inverse Beta Decay or IBD(^{63}Cu) potassium energy region [1.176, 1.311] MeV are $S_{IBD(Cu)}(K) = 0.10$ TNU, $S_{IBD(Cu)}(U + Th) = 1.9{\cdot}10^{-2}$ TNU, $S_{IBD(Cu)}$ (reactors) = $1.9{\cdot}10^{-3}$ TNU, as summarised in Table 3. The expected geoneutrino signal and the irreducible reactor and geoneutrino background in the IBD(p) energy region [1.806, 3.272] MeV are $S_{IBD(p)}(U + Th) = 40.6$ TNU, $S_{IBD(p)}$(reactors) = 22.2 TNU[56]. The $S_{IBD(p)}(U + Th)$ estimate is ~6 TNU higher with respect to ref. 14, which adopts U and Th abundances inferred from local samplings[68] and did not report K in the sedimentary deposits of the Apennines chain; here we calculated the expected geoneutrino signal using the global model of ref. 50. Two hypothetical Cu mass loadings are considered, 50% and 10% (green and blue lines, respectively), defined as the ratio between the Cu mass and the overall detector mass. **a** shows the ^{40}K geoneutrino detection significance in number of σ and is calculated by conservatively considering a +1σ statistical uncertainty on the number of IBD(p) events, which is propagated in the estimation of the background events in the ^{63}Cu potassium energy region ($\mu + \Delta\mu$), as defined in Eq. 1. Each data point corresponds to an integer number of events N observed in the ^{63}Cu potassium energy region. **b** shows the statistical uncertainty on the IBD(p) (U + Th) geoneutrino signal, which is estimated as the square root of the number of geoneutrino plus reactor IBD(p) events.

measure the U and Th geoneutrino (and reactor) fluxes, as backgrounds. Those neutrons are tagged by either the 2.2 MeV gamma ray following neutron capture by protons or by the energetic multiple gamma rays released following neutron capture by either of the stable isotopes of copper, ^{63}Cu or ^{65}Cu. If the neutron is missed, for example by undergoing (n, p) or (n, α) on Cu, with the final state particles not detected, it must be accounted for in the IBD(p) efficiency and as a potential ^{40}K geoneutrino background if the e^+ signal is in accidental coincidence with another event resembling an 87 keV point energy deposition—the latter is likely to be a very rare occurrence.

As shown in Fig. 5, the significance of the ^{40}K geoneutrino signal detection reaches the level of 5 (3) sigma for a detector mass slightly under 240 (90) kilotons and 50% copper-loading, with 10 years of data taking. Details are shown in Table 3. Despite the robustness of the detection methodology being proposed, the discovery potential for potassium geoneutrinos remains a major experimental challenge due to the small event rate of K geoneutrinos. Even in a hypothetical background-free scenario, this is largely unavoidable as it is due to the small acceptance caused by the narrow detection energy window, [1.0, 1.3] MeV for charged-current interactions, and the cross sections involved. The discovery of K geoneutrinos via this methodology, if proven feasible, would require a detector mass comparable to that of Hyper-Kamiokande[40] even in the optimistic – experimentally not demonstrated—scenario where doping is postulated at the 50% level. LiquidO detector technology and its positron detection signature would help achieve the necessary, enormous background suppression. The delayed coincidence with the ^{63}Ni* deexcitation gamma ray is another strong feature, adding robustness to the overall methodology. Discussion of the practicality of such a detector can be found in the 'Methods' section.

Figure 5 illustrates two loading cases for comparison: 10% and 50%, by weight fraction. Loading at 10% represents what has been previously achieved in liquid scintillator experiments (e.g. LENS R&D[41]), corresponding to the present state-of-the-art. High loading above ≥10% would require further vigorous R&D effort. In any case, maximising the light yield of the scintillator cocktail is important due to the low kinetic energy of the e^+ originating from IBD(^{63}Cu), depositing no more than ~100 keV energy. For the detection of the e^+, both annihilation gamma rays are readily observed and can be traced back to their common point of origin. Nevertheless, registering the signal from the energy deposited by the e^+ (the event pattern centre) and the 87 keV γ sets the target for detector light collection to be a minimum of around 200 photoelectrons/MeV, corresponding to ~20 photoelectrons for these energies, so as to preserve good pattern recognition and sensitivity to these low energy events.

Despite the enormous challenges posed by this problem, the methodology and basic concepts of our proposed approach to K geoneutrino discovery are sound, with a development path that can be based on experiment. Prototypes are being developed that could eventually test a copper-doped scintillator deployed close to a nuclear reactor[42]. The same technique for testing ^{40}K geoneutrino detection can also detect lower-energy reactor antineutrinos that haven't previously been observed by IBD(p) reactions, and from spent nuclear fuel. In this way, reactors may be used as effective 'test-beam' facilities to experimentally demonstrate much of the described methodology. Our work is not a proposal for a specific experiment but rather aimed to fully explore what it would take to pursue K geoneutrino detection using a charged-current interaction, exploiting the distinctive antimatter signature of geoneutrino events, thus providing the framework for fully envisaging this exciting possibility.

Conclusions

In this article, we propose to use charged-current antineutrino interactions on ^{63}Cu to detect ^{40}K geoneutrinos, featuring the e^+ (antimatter) tagging ability of the LiquidO detection technique. ^{63}Cu has been identified as the ideal isotope due to its large natural abundance, relatively high cross section and robustness to numerous e^+ backgrounds that were considered. A huge LiquidO scintillation detector of about 240 (90) kilotons mass with 50% Cu loading appears to be the minimal configuration to reach 5 (3) sigma discovery potential upon 10 years of exposure. In the same detector, the simultaneous detection of U and Th geoneutrinos using conventional IBD interactions on protons would yield a high statistical sample (of order 35,000 events), leading to a permille-level statistical precision of the U and Th geoneutrino fluxes. Such precise measurements, combined with direct knowledge from ^{40}K geoneutrinos, would be insightful for discriminating

between competing models of Earth's chemical composition and the distribution of the main heat-producing elements (U, Th and K)[43].

The challenge of building such an enormous detector is clear. While LiquidO technology is at an early level of development, including the highly doped liquid scintillator, most of the experimental feasibility of the methodology could be established via dedicated data-driven 'test-beam' measurements using a small LiquidO detector of a few-tons scale, located close to a nuclear reactor, similar to that foreseen in the CLOUD/AntiMatter-OTech scientific programme[42].

Our complete understanding of the Earth and its formation would greatly benefit from the observation of ^{40}K geoneutrinos, whose rate measurement would constitute a major discovery. The impact of the first ^{40}K geoneutrino measurement would be a direct determination of the bulk mass of potassium in the Earth and its abundance in the deep interior, after accounting for the actual knowledge of the amount of potassium in the accessible lithosphere. Current geoneutrino measurements provide radiogenic heat estimates relying on a model-dependent K/U ratio. Instead, a direct measurement of the ^{40}K heat power would provide an experimental constraint to the radiogenic fraction of Earth's internal heat budget. For instance, a fully chondritic Earth would produce a very large ^{40}K signal[44]; hence confirmation of such an Earth model would be possible. Moreover, measuring the K/U ratio would also provide critical information about the behaviour of volatile elements during Earth's early-stage formation[45]. The detector being proposed would provide a precise measurement of the Th/U ratio in the bulk Earth, another quantity that tests bulk composition assumptions based on chondritic models. Finally, a direct measurement of the ^{40}K geoneutrinos would be crucial to shed light on the missing K and Ar mysteries and, in turn, provide insights into Earth's composition, structure, and thermal evolution. The K geoneutrino discovery stands as one of the most important quests and challenges in this field of research today.

Methods

Geoneutrino signal calculation

The prediction of the IBD geoneutrino signal at a given experimental site requires the modelling of the three geoneutrino life-stages, i.e. (i) production inside the Earth, (ii) propagation to the detector site and (iii) detection via the IBD reaction on a given target.

For a given Earth elemental volume, U, Th and K activities (i.e. the average decay rates) are separately computed as the ratio between the number of radioactive nuclei and the corresponding radioisotope mean lifetime. The oscillated geoneutrino flux is obtained by weighting the activities for the corresponding geoneutrino spectrum (normalised to the number of geoneutrinos per decay)[9,46], by scaling for the isotropic $1/4\pi r^2$ spherical factor, and by applying the electron antineutrino three-flavour survival probability[47] with up-to-date oscillation parameters[48]. Finally, the U, Th and K geoneutrino IBD signals per unit time and unit target isotope are calculated by convolving the oscillated geoneutrino spectra with the IBD cross section for the target isotope of interest. Expected signals in Terrestrial Neutrino Units (TNU) are determined by assuming a one-year acquisition time and 10^{32} IBD target nuclei as follows[9,49]:

$$S_{i,n}(\vec{r}) = \frac{IA_n N_{\text{target}} \cdot T}{m_i \cdot \tau_i} \cdot \int dE_{\bar{\nu}} \cdot \text{Sp}_i\left(E_{\bar{\nu}}\right) \cdot \sigma_n\left(E_{\bar{\nu}}\right) \int d^3r' \cdot \frac{C_i \cdot a_i(\vec{r}') \cdot \rho(\vec{r}')}{4\pi|\vec{r}-\vec{r}'|^2} \cdot P_{ee}\left(E_{\bar{\nu}}, |\vec{r}-\vec{r}'|\right)$$

where i runs over the HPE (i = ^{238}U, ^{232}Th and ^{40}K) and n runs over the target isotope (n = ^{1}H, ^{3}He, ^{14}N, ^{33}S, ^{35}Cl, ^{45}Sc, ^{63}Cu, ^{79}Br, ^{87}Sr, ^{93}Nb, ^{106}Cd, ^{107}Ag, ^{135}Ba, ^{147}Sm, ^{151}Eu, ^{155}Gd, ^{171}Yb and ^{187}Os), IA_n is the isotopic abundance of the IBD target isotope, N_{target} is equal to 10^{32}, T is a one-year acquisition time [s], m_i is the atomic mass of the HPE [g], τ_i is the mean lifetime of the HPE [s], $\text{Sp}_i\left(E_{\bar{\nu}}\right)$ is the geoneutrino energy spectrum for the *i-th* HPE [$\#\bar{\nu}$ MeV^{-1}], $\sigma_n\left(E_{\bar{\nu}}\right)$ is the IBD cross section for the n-th target isotope [cm^2], C_i is the isotopic abundance of the *ith* HPE [g/g], $a_i(\vec{r}')$ is the mass abundance [g/g] of the *ith* HPE in the elemental volume d^3r', $\rho(\vec{r}')$ is the volumetric density of the elemental volume d^3r'[g/cm^3], $\vec{r}$ is the position of the experimental site with respect to the centre of the Earth, $\vec{r}'$ is the position of the elemental volume d^3r' with respect to the centre of the Earth and $P_{ee}\left(E_{\bar{\nu}}, |\vec{r}-\vec{r}'|\right)$ is the electron antineutrino survival probability [dimensionless] for an antineutrino with energy $E_{\bar{\nu}}$ travelling for a distance $|\vec{r}-\vec{r}'|$ [cm] from the emission point in the elemental volume to the detector position.

In order to perform this geoneutrino signal calculation, it is necessary to adopt a 3-dimensional voxel-wise Earth model according to which each elemental volume is assigned with an HPE abundance and a volumetric density. At this scope, the Earth is typically divided into its two main HPEs-bearing reservoirs, i.e. the lithosphere (shallow and relatively rich in HPEs) and the mantle (thick and relatively poor in HPEs)[50]. The lithosphere is the outermost Earth shell with an average thickness of 170 km, comprising (from top to bottom) sediments, continental or oceanic crust and continental lithospheric mantle, while the mantle has a typical thickness of 2800 km and extends from the bottom of the lithosphere to the core-mantle boundary.

The geophysical structure of the Earth is quite well established from seismic and gravimetric measurements both in terms of reservoir thicknesses and density[50]; on the other hand, a wide range of compositional models of the Bulk Silicate Earth (BSE) has been proposed in the past decades. In particular, three of the most popular classes of BSE compositional models are typically referred to as 'cosmochemical', 'geochemical' and 'geodynamical', which are respectively based on EH enstatite chondrites composition (low HPE abundances), CI carbonaceous chondrites composition (moderate HPE abundances) and on the energetics of mantle convection and the observed surface heat loss (high HPE abundances)[42]. Following[14], in the panorama of available compositional models, we call 'cosmochemical' the model of ref. 51, 'geochemical' the model of ref. 1 with K abundances corrected following ref. 52 and 'geodynamical' the model of ref. 53, which provides the HPE masses in the BSE (M_{BSE}) reported in Table 4.

In the context of possible HPE distributions in the Earth, we rely on the fact that for each HPE, the average mass in the lithosphere (M_{litho}), together with its standard deviations (σ_{litho}), is statistically well known from direct measurements on rock samples[50]. In this perspective, subtracting M_{litho} from the M_{BSE}, the residual HPE masses are assigned to the mantle ($M_{\text{mantle}} = M_{\text{BSE}} - M_{\text{litho}}$) according to 3 different possible distributions: (i) in a 10 km thick layer at the core-mantle boundary[54], (ii) in a 710 km thick enriched mantle layer sitting at the core-mantle boundary and underlying a 2090 km thick depleted mantle[50], (iii) in a 2800 km thick homogeneous mantle[55]. The core is considered devoid of HPEs.

Across the possible combinations of HPE masses and distributions, a 'low', 'medium' and 'high' scenario were built by taking into account the following points: (i) the geophysical structure of the reservoirs belonging to the lithosphere is fixed and taken after[14]; (ii) the lithospheric HPE masses can vary in the σ_{litho} range (iii) the 'proximity argument' holds[9], which states that 'the minimal (maximal) contributed flux is obtained by placing HPE as far (close) as possible to the detector'. Supplementary Fig. 1 and Supplementary Table 1 provide, respectively, a visual sketch and a quantitative description of the relevant features of the 'low', 'medium' and 'high'

Table 4 | Bulk silicate Earth compositional models

	M_{BSE}(U) [10^{16} kg]	M_{BSE}(Th) [10^{16} kg]	M_{BSE}(K) [10^{19} kg]
Cosmochemical	5 ± 1	17 ± 2	59 ± 12
Geochemical	8 ± 2	32 ± 5	113 ± 24
Geodynamical	14 ± 2	57 ± 6	142 ± 14

Uranium, thorium and potassium masses in the BSE (i.e. actual lithosphere plus mantle reservoirs) for the 'cosmochemical', 'geochemical' and 'geodynamical' models adopted in the present study and taken from ref. 14. HPE masses for the BSE are calculated multiplying each HPE expected abundance by the BSE bulk mass of 4.035 × 10^{24} kg. The "cosmochemical" BSE abundances are taken from ref. 42 and based on the enstatite BSE model of ref. 51. The 'geochemical' BSE abundances are taken from ref. 1 with some minor corrections for the K abundances taken after ref. 45. Finally, the "geodynamical" BSE abundances are taken from ref. 42, which is based on[67] estimates.

scenarios that give rise to, respectively, the minimum, central and maximum geoneutrino fluxes and signals (see also Fig. 1 and Table 1), defining the expected signal and its variability range. The resulting HPEs masses adopted for the signal calculation for the three different scenarios are reported in Supplementary Table 2.

The above-mentioned methodology is followed in this work to calculate the geoneutrino signals, and their variability ranges, on different IBD targets expected at Laboratori Nazionali del Gran Sasso (LNGS: 42.45°N, 13.57°E), as a pertinent example site where much information exists. For the sake of completeness, we underline that the intensity of the signal strongly depends on the experimental site position. Provided that the mantle contribution is isotropic, the following arguments need to be considered: (i) although the average crustal thickness is about 35 km, it can range from ~5 km (thinnest oceanic crust) up to ~70 km (thickest continental crust); (ii) the continental crust is richer in HPE (~40 times higher mass abundances) compared to the oceanic crust. In this framework, LNGS, sitting on top of ~35 km continental crust, represents an intermediate case. Two extreme examples of 'oceanic' and 'continental' geoneutrino potential experimental sites could be represented by Hawaii (19.72°N, 156.32°W) and the Himalayas (33.00°N, 85.00°E), respectively. Indeed, according to the 'medium' scenario, at a Himalayan site, the geoneutrino signal ($S_{IBD(p)}(U+Th) = 58$ TNU) is expected to be generated by HPE distributed in the lithosphere with a fraction of about 85%, while at Hawaii, approximately 75% of the geoneutrino signal ($S_{IBD(p)}(U+Th) = 12$ TNU) originates from the mantle[50].

Reactor antineutrino signal calculation

The expected reactor signal at LNGS, as an example site, was estimated as the superposition of the signals generated by all commercial nuclear power plants[56], where the parameterised antineutrino spectral shape[57] per decay was adopted to extrapolate the reactor spectrum down to the ^{40}K geoneutrino energy window. In this respect, LNGS represents an experimental location with a long 'baseline', as the closest commercial reactor is at ~400 km distance and produces the largest signal fraction (only ~3% of the total reactor signal). The annual expected reactor neutrino signal is almost constant (as each distant reactor provides only a small fraction of the signal, hence variations due to any given core's operation are not so significant) and provides about 35% of the IBD(p) signal in the geoneutrino energy window [1.806, 3.272] MeV and a small (~1%) fraction of the IBD(^{63}Cu) signal in the ^{40}K geoneutrino energy window [1.176, 1.311] MeV.

Inverse beta decay cross-section calculation and expected geoneutrino spectra

The nuclear matrix element for an antineutrino capture reaction $\bar{\nu}_e + {}_Z^AX \rightarrow e^+ + {}_{Z-1}^AY$ is similar to the one from the related β decay ${}_{Z-1}^AY \rightarrow {}_Z^AX + e^- + \bar{\nu}_e$ and can be derived from its ft value, or comparative half-life, which typically provides a useful criterion for the classification of radioactive transitions as allowed or forbidden to various degrees. The antineutrino capture reaction has a target dependent energy threshold $E_{th} = Q_\beta + 2m_e$, where Q_β is the total energy released in ${}_{Z-1}^AY$ nuclear β decay.

The total charged current cross section (in natural units) can be calculated directly from evaluating the appropriate β-decay reaction and correcting for the spin of the system as follows[58]:

$$\sigma = \frac{2\pi^2 \ln 2}{ft\, m_e^5} p_e E_e F\left(E_e, Z_f\right) \frac{(2J_f+1)}{(2J_i+1)}$$

where ft is the comparative half-life of the β decaying nucleus, taken from the ENDSF nuclear database[59], m_e, p_e and $E_e = E_{\bar{\nu}_e} - E_{th} + m_e$ are, respectively, the e^+ mass, momentum and total energy; $F(E_e, Z_f)$ is the Fermi nuclear function correcting for Coulomb repulsion between the e^+ and the nucleus of the final state having charge $Z_f = Z - 1$; $\frac{(2J_f+1)}{(2J_i+1)}$ is the spin correction factor for a final state with spin J_f and initial state with spin J_i.

In view of ^{40}K geoneutrino detection via the antineutrino capture reaction, the target isotope candidates were selected considering the following constraints: (i) $E_{th} < 1.311$ MeV, and (ii) relatively low ft values (i.e. relatively high cross section). The Nuclear Data Section of the IAEA provides a user-friendly API that can be used to query nuclear data and investigate isotope properties. According to the Evaluated Nuclear Structure Data File (ENSDF), contained in the IAEA database[59], a total of 515 different β^- emitters exist for a total of 523 possible transitions to ground state. We are interested in these β^- decaying isotopes since their products are suitable targets for the inverse process, namely the IBD. Among these 515 emitters, we are interested in those having a threshold at $E_{th} < 1.311$ MeV, the energy endpoint of the ^{40}K geoneutrino spectrum. There are a total of 26 possible targets satisfying this condition, not all, however, are stable. Since a realistic geoneutrino experiment will require a large number of target nuclei and a high level of radiopurity, this consideration is sufficient of itself alone to discard all the unstable candidates. We thus discuss only targets which are stable or can be considered stable on the time scale of a geoneutrino experiment (such as the ones having half-lives comparable or higher than Earth's age, ^{151}Eu and ^{147}Sm), ending up with a total of 17 targets leading to 20 possible IBD transitions. This led to the identification of 17 target isotopes: ^{3}He, ^{14}N, ^{33}S, ^{35}Cl, ^{45}Sc, ^{63}Cu, ^{79}Br, ^{87}Sr, ^{93}Nb, ^{106}Cd, ^{107}Ag, ^{135}Ba, ^{147}Sm, ^{151}Eu, ^{155}Gd, ^{171}Yb and ^{187}Os, shown in Supplementary Table 3, and Supplementary Fig. 2.

Candidates with low E_{th} values and with possible allowed transitions to an excited state are ^{63}Cu, ^{79}Br and ^{151}Eu. The $\bar{\nu}_e$ reaction energy threshold must include the energy of the excited state and still be below the ^{40}K geoneutrino spectrum endpoint; that is the case for all three of these isotopes and their possible (allowed) excited states. However, only an approximate value of Log(ft) = 5[22] is assumed for the excited states, with an admissible range of 4–6 (with some even larger values occurring)[60]. Indeed, while for ^{79}Br → ^{79}Se* the Log(ft) value can be analytically estimated (using the ^{79}Se* → ^{79}Br branching ratio, its half-life and the Fermi functions of the two states), for ^{63}Cu → ^{63}Ni* and ^{151}Eu → ^{151}Sm* the lack of knowledge of the branching ratio and/or the half-life of the final state prohibits a Log(ft) calculation. As the cross section is inversely proportional to ft, a 2-unit change in Log(ft) will result in a 2 orders of magnitude variation in the cross section. Even a small (10%) increase (decrease) in Log(ft) will provide a cross section that is reduced (enhanced) by a factor 3 with respect to the central value estimate. This large uncertainty calls for refined nuclear physics input coming from theory and/or experiments, in particular for ^{63}Cu, which is the most promising candidate. Measurements using nuclear reactor neutrinos, as a source, would enable a direct calibration of the ^{63}Cu cross section for geoneutrino detection relative to the IBD(p) interaction.

^{3}He would be an excellent target with a high cross section (low ft) and one of the lowest energy thresholds. However, its scarcity (1.3×10^{-4}% isotopic abundance) and extremely high cost would make its choice prohibitive. Similar arguments apply to ^{106}Cd, ^{33}S, which would require isotopic enrichment to increase isotopic abundance from the natural 1.25% and 0.75%. Moreover, only an upper limit for the ^{106}Ag → ^{106}Cd beta decay branching ratio is available (BR < 1%[59]), limiting the knowledge of ^{106}Cd cross section to an estimated maximum value (Log(ft) > 4.1). For ^{45}Sc, ^{79}Br, ^{87}Sr, ^{135}Ba, ^{147}Sm, ^{151}Eu and ^{155}Gd the energy threshold is too close to the ^{40}K endpoint to enable the detection of a relevant portion of the spectrum (Supplementary Table 3). Although ^{14}N is characterised by low Z (i.e. small Fermi Coulomb correction) and by a ~ 100% isotopic abundance, the allowed β decay is disfavoured (high ft value). This makes ^{14}N a poor target choice due to its small antineutrino cross section. A similar argument applies to ^{93}Nb, ^{171}Yb, ^{107}Ag and ^{187}Os, whose poor ft values strongly limit the amplitude of the IBD cross section, excluding them as possible targets. In conclusion, ^{35}Cl and ^{63}Cu were identified as the most promising antineutrino capture target for the detection of ^{40}K geoneutrinos.

Detector considerations, challenges and experimental development

Our study concluded that a detector at the scale of 100–200 kilotons, doped with copper at 50% by weight, would be required to achieve sufficient signal detection significance for the discovery of ^{40}K geoneutrinos. The purpose of

our study was not a proposal for an experiment but a comprehensive examination of the signal and background characteristics for ^{40}K geoneutrino detection using charged-current interactions on all possible, practical (high natural abundance) nuclear targets. Nevertheless, we address several of the main practicalities associated with building such a detector in the discussion that follows.

Size—At 240 kilotons, required for a 5-sigma discovery (10 years of data), the detector would be comparable in size to Hyper-Kamiokande[40]. At 90 kilotons (for a 3-sigma discovery), the size would be similar in scale to DUNE[61]. Since LiquidO technology is required for e^+ identification, its scalability is at stake and reaching such a detector mass is a non-negligible challenge with today's technology. LiquidO detector size scaling is currently limited by fibre attenuation, imposing a limit along one detector dimension (along the length of the fibre). Overall detector size, transverse to the direction of the fibres, is also restricted by the need for overburden (and an underground location) to reduce cosmogenic backgrounds, as discussed in the main article. For now, the SuperChooz project[62], with a 10-kiloton mass and LiquidO technology, is under consideration, realisable as it is comparable in size and scale with the existing NOvA detector[63]. However, projecting a further increase in size by an order of magnitude, likely requiring improvements in fibre technology beyond today's state of the art, would indeed be a formidable challenge.

Cost—The price of copper today (for 45,000 tons or more) would amount to several hundred million USD. Other components that are expensive and that scale with size include the liquid scintillator and optical fibres. Using NOvA as the closest analogue for a LiquidO ^{40}K geoneutrino detector, the greater fibre density needed for LiquidO would necessitate 6 times as many fibres, and the size scaling factor would multiply by roughly another factor of 17. Hence, the total scaling factor for the cost of optical fibres would be a factor of 100 going from NOvA scale to that needed for ^{40}K geoneutrino detection. Offsetting this potentially is the benefit of the 'self-segmentation' provided by LiquidO. With no segmentation cells to build (as in NOvA), there would be potential cost savings for the overall scintillator container.

Liquid scintillator—The main article emphasised that high-level copper doping at 50% requires dedicated R&D. The fact that LiquidO scintillator is deliberately highly scattering (in its opacity) means that numerous approaches for achieving high doping have been identified and are under development. The properties of the scintillator and wavelength-shifting fibres are also important, and we stress that high light yield is a requirement given the low kinetic energy deposited by the produced e^+ prompt signal and the coincident 87 keV gamma ray.

Complexity—Increasing the number of readout channels does not necessarily increase complexity, especially in the modern era of ASIC-based electronics and deep learning for data analysis. However, the mechanical complexity in the deployment of a large grid of fibres implies unexplored engineering challenges. Again, dedicated scaling R&D will be required to address these questions.

Prototyping—While other physics experiments can progressively increase sensitivity, achieving results with each milestone, to commit to such a large-scale 'moon-shot' endeavour would not be realistic if there were not a programme that would provide scientific progress and results along the way. The challenges can be met on the experimental side as novel solutions (e.g. for doping, fibres, mechanics, etc.) are developed and scaled up. Proof-of-principle demonstrations are envisioned in the CLOUD[41] programme that includes (Cu) doped scintillator deployed close to powerful nuclear reactors. Signal detection methodology traits (such as the Ni deexcitation gamma in coincidence) can be refined and the cross section measured experimentally (confirming calculations) by following a progression of experiments that would ultimately lead to the enormous undertaking of a ^{40}K geoneutrino discovery instrument. As the IBD(Cu) reaction cross section has not been experimentally observed, measuring it is the highest priority, as all other considerations (discussed above), such as detector size, cost and complexity, scale inversely with the unknown cross section.

Data availability

Data sharing is not applicable to this article as no datasets were generated or analysed during the current study.

Received: 13 May 2024; Accepted: 20 January 2026;
Published online: 09 February 2026

References

1. McDonough, W. F. & Sun, S. -S. The composition of the Earth. *Chem. Geol.* **120**, 223–253 (1995).
2. Davies, J. H. & Davies, D. R. Earth's surface heat flux. *Solid Earth* **1**, 5–24 (2010).
3. McDonough, W. F., Šrámek, O. & Wipperfurth, S. A. Radiogenic power and geoneutrino luminosity of the earth and other terrestrial bodies through time. *Geochem. Geophys. Geosyst.* **21**, e2019GC008865 (2020).
4. Arevalo, R. et al. Simplified mantle architecture and distribution of radiogenic power. *Geochem. Geophys. Geosyst.* **14**, 2265–2285 (2013).
5. Goettel, K. A. Models for the origin and composition of the Earth, and the hypothesis of potassium in the Earth's core. *Geophys. Surv.* **2**, 369–397 (1976).
6. Lassiter, J. C. Role of recycled oceanic crust in the potassium and argon budget of the Earth: Toward a resolution of the "missing argon" problem. *Geochem. Geophys. Geosyst*. **5**, Q11012 (2004).
7. Allègre, C. J., Hofmann, A. & O'Nions, K. The argon constraints on mantle structure. *Geophys. Res. Lett.* **23**, 3555–3557 (1996).
8. Marty, B. The origins and concentrations of water, carbon, nitrogen and noble gases on Earth. *Earth Planet. Sci. Lett.* **313**, 56–66 (2012).
9. Fiorentini, G., Lissia, M. & Mantovani, F. Geo-neutrinos and Earth's interior. *Phys. Rep.* **453**, 117–172 (2007).
10. Raghavan, R. S. et al. Measuring the global radioactivity in the Earth by multidetector antineutrino spectroscopy. *Phys. Rev. Lett.* **80**, 635 (1998).
11. Rothschild, C. G., Chen, M. C. & Calaprice, F. P. Antineutrino geophysics with liquid scintillator detectors. *Geophys. Res. Lett.* **25**, 1083–1086 (1998).
12. KamLAND Collaboration. Measurement of neutrino oscillation with KamLAND: evidence of spectral distortion. *Phys. Rev. Lett*. **94**, 081801 (2005).
13. Agostini, M. et al. Spectroscopy of geoneutrinos from 2056 days of Borexino data. *Phys. Rev. D* **92**, 031101 (2015).
14. Agostini, M. et al. Comprehensive geoneutrino analysis with Borexino. *Phys. Rev. D* **101**, 012009 (2020).
15. Albanese, V. et al. The SNO+ experiment. *J. Instrum.* **16**, P08059 (2021).
16. An, F. et al. Neutrino physics with JUNO. *J. Phys. G Nucl. Part. Phys.* **43**, 030401 (2016).
17. Leyton, M., Dye, S. & Monroe, J. Exploring the hidden interior of the Earth with directional Neutrino measurements. *Nat. Commun.* **8**, 15989 (2017).
18. Wang, Z. & Chen, S. Hunting potassium geoneutrinos with liquid scintillator Cherenkov Neutrino detectors. *Chin. Phys. C* **44**, 033001 (2020).
19. Benziger, J. et al. A scintillator purification system for the Borexino solar Neutrino detector. *Nucl. Instrum. Methods Phys. Res. A Accel. Spectrom. Detect. Assoc. Equip.* **587**, 277–291 (2008).
20. Cowan, C. L. et al. Detection of the free neutrino: a confirmation. *Science* **124**, 103–104 (1956).
21. Abreu, Y. et al. SoLid: a short baseline reactor Neutrino experiment. *J. Instrum.* **16**, P02025 (2021).
22. Krauss, L. M., Glashow, S. L. & Schramm, D. N. Antineutrino astronomy and geophysics. *Nature* **310**, 191–198 (1984).
23. Chen, M. *Potassium Geo-neutrino Detection*. as presented at *Neutrino Geophysics 2005*, Honolulu, HI, USA (2005).

24. Cabrera, A. et al. Neutrino physics with an opaque detector. *Commun. Phys.* **4**, 273 (2021).
25. Schoppmann, S. Review of novel approaches to organic liquid scintillators in neutrino physics. *Symmetry* **15**, 11 (2023).
26. Apilluelo, J. et al. The stochastic light confinement of LiquidO. Preprint at arXiv https://doi.org/10.48550/arXiv.2503.02541 (2025).
27. Cabrera, A. & LPET-Otech Collaboration, Novel positron emission tomography with opaque liquid scintillator detection technology. In *Proc. 2022 IEEE Nuclear Science Symposium, Medical Imaging Conference and Room Temperature Semiconductor Detector Conference (NSS-MIC-IEEE)* (IEEE,2022).
28. Honda, M. et al. Atmospheric neutrino flux calculation using the NRLMSISE-00 atmospheric model. *Phys. Rev. D* **92**, 023004 (2015).
29. Bellini, G. et al. Geoneutrinos and geoscience: an intriguing joint-venture. *Riv. Nuovo Cim.* **45**, 1–105 (2022).
30. Abe, S. et al. Measurement of cosmic-ray muon spallation products in a xenon-loaded liquid scintillator with KamLAND. *Phys. Rev. C* **107**, 054612 (2023).
31. Berger, M. et al. *XCOM: photon cross sections database: NIST standard reference database 8* (NIST, 2013).
32. Karshenboim, S. G. Precision study of positronium: testing bound state QED theory. *Int. J. Mod. Phys. A* **19**, 3879–3896 (2004).
33. Franco, D., Consolati, G. & Trezzi, D. Positronium signature in organic liquid scintillators for neutrino experiments. *Phys. Rev. C* **83**, 015504 (2011).
34. Consolati, G. et al. Characterization of positronium properties in doped liquid scintillators. *Phys. Rev. C* **88**, 065502 (2013).
35. Abe, Y. et al. Ortho-positronium observation in the double Chooz experiment. *J. High Energy Phys.* **2014**, 32 (2014).
36. Firestone, R. et al. *Database of prompt gamma rays from slow neutron capture for elemental analysis* (IAEA Publications, 2004).
37. Beckurts, K.-H. & Wirtz, K. *Neutron Physics* (Springer Science & Business Media, 2013).
38. Newsome, I., Bhike, M. & Tornow, W. J. Neutron radiative capture cross section of Cu 63, 65 between 0.4 and 7.5 MeV. *Phys. Rev. C* **97**, 044617 (2018).
39. Bityukov, S. I. & Krasnikov, N. V. Signal significance in the presence of systematic and statistical uncertainties. *J. High. Energy Phys.* **2002**, 060 (2002).
40. Abe, K. et al. *Hyper-Kamiokande design report*. https://doi.org/10.48550/arXiv.1805.04163 (2018).
41. Raghavan, R. S. New prospects for real-time spectroscopy of low energy electron neutrinos from the sun. *Phys. Rev. Lett.* **78**, 3618 (1997).
42. Cabrera, A. (CLOUD Collaboration). CLOUD: a new generation of neutrino science at Chooz. *XXth International Workshop on Neutrino Telescopes (NeuTel)*, Venice, Italy (2023) on Zenodo https://doi.org/10.5281/zenodo.10049846.
43. Šrámek, O. et al. Geophysical and geochemical constraints on geoneutrino fluxes from Earth's mantle. *Earth Planet. Sci. Lett.* **361**, 356–366 (2013).
44. Fiorentini, G. et al. KamLAND, terrestrial heat sources and neutrino oscillations. *Phys. Lett. B* **558**, 15–21 (2003).
45. Arevalo, R., McDonough, W. F. & Luong, M. The K/U ratio of the silicate Earth: insights into mantle composition, structure and thermal evolution. *Earth Planet. Sci. Lett.* **278**, 361–369 (2009).
46. Enomoto, S. Geoneutrino Spectrum and Luminosity. Database: https://www.awa.tohoku.ac.jp/~sanshiro/research/geoneutrino/spectrum/ (2006).
47. Capozzi, F., Lisi, E. & Marrone, A. Neutrino mass hierarchy and electron neutrino oscillation parameters with one hundred thousand reactor events. *Phys. Rev. D* **89**, 013001 (2014).
48. Capozzi, F. et al. *Current unknowns in the three-neutrino framework* (Progress in Particle and Nuclear Physics, 2018).
49. Strati, V. et al. Perceiving the crust in 3-D: a model integrating geological, geochemical, and geophysical data. *Geochem. Geophys. Geosyst.* **18**, 4326–4341 (2017).
50. Huang, Y. et al. A reference Earth model for the heat-producing elements and associated geoneutrino flux. *Geochem. Geophys. Geosyst.* **14**, 2023–2029 (2013).
51. Javoy, M. et al. The chemical composition of the Earth: enstatite chondrite models. *Earth Planet. Sci. Lett.* **293**, 259–268 (2010).
52. Arevalo, R. & McDonough, W. F. Chemical variations and regional diversity observed in MORB. *Chem. Geol.* **271**, 70–85 (2010).
53. Turcotte, D. & Schubert, G. *Geodynamics* (Cambridge University Press, 2014).
54. KamLAND Collaboration. Reactor on-off antineutrino measurement with KamLAND. *Phys. Rev. D* **88**, 033001 (2013).
55. Enomoto, S. et al. Neutrino geophysics with KamLAND and future prospects. *Earth Planet. Sci. Lett.* **258**, 147–159 (2007).
56. Baldoncini, M. et al. Reference worldwide model for antineutrinos from reactors. *Phys. Rev. D* **91**, 065002 (2015).
57. Mueller, T. A. et al. Improved predictions of reactor antineutrino spectra. *Phys. Rev. C* **83**, 054615 (2011).
58. Formaggio, J. A. & Zeller, G. P. From eV to EeV: Neutrino cross sections across energy scales. *Rev. Mod. Phys.* **84**, 1307 (2012).
59. ENSDF database as of May 7, 2023. Version available at http://www.nndc.bnl.gov/ensarchivals/.
60. Fukugita, M. & Yanagida, T. *Physics of Neutrinos: and Application to Astrophysics* (Springer Science & Business Media, 2013).
61. Abi, B. et al. *Deep Underground Neutrino Experiment (DUNE), Far Detector Technical Design Report, Volume I: Introduction to DUNE*. FERMILAB-PUB-20-024-ND (CERN, 2020).
62. Cabrera, A. The SuperChooz experiment: unveiling the opportunity. In *Proc. CERN EP Seminar* (CERN, 2022).
63. Ayres, D. S. et al. *The NOvA Technical Design Report*. FERMILAB-DESIGN-2007-01 (Fermilab, 2007) https://doi.org/10.2172/935497.
64. Singh, B. Nuclear Data Sheets for A=1. *Nucl. Data Sheets* **106**, 601–618 (2005).
65. Chen, J., Cameron, J. & Singh, B. Nuclear data sheets for A=35. *Nucl. Data Sheets* **112**, 2715–2850 (2011).
66. De Frenne, D. & Negret, A. Nuclear Data Sheets for A=106. *Nucl. Data Sheets* **109**, 943–1102 (2008).
67. Turcotte, D. L. & Schubert, G. *Geodynamics, applications of continuum physics to geological problems*, Second edition (Cambridge University Press, 2002).
68. Coltorti, M. et al. U and Th content in the Central Apennines continental crust: a contribution to the determination of the geo-neutrinos flux at LNGS. *Geochim. Cosmochim. Acta* **75**, 2271–2294 (2011).

Acknowledgements

We acknowledge the support received from: (i) the 'Chaire Internationale de Recherche Blaise Pascal' (Laureate 2016: F. Suekane), financed by Région Île-de-France (Paris) and coordinated by the Fondation de l'École Normale Supérieure (Paris) and hosted by CNRS at the APC Laboratory (Paris). This funding enabled launching the pioneering studies, including supporting a dedicated postdoctoral research fellow (S. Wagner) whose studies, input and comments were critical; (ii) 'L'Instituto Universitario de Studi Superiori-Ferrara 1391' for supporting Copernicus Visiting Scientist (Laureate 2019: M. Chen) and hosted by the Università di Ferrara and INFN Ferrara during the key phase of this study; and (iii) the 'Emilie du Châtelet' Programme, financed by the P2IO (LabEx, Université Paris-Saclay, France) supporting visiting scientist (2022: M. Chen) hosted at the IJCLab during the final writeup phase of this publication. We also thank Prof C. Volpe (APC, Paris) for helpful discussions regarding nuclear physics input for neutrino cross sections. The authors pay tribute to Prof Giovanni Fiorentini for his pioneering studies on geoneutrinos. Although he passed away in June 2022, his memory remains vibrant in our minds.

Author contributions

The primary authors for this work have been listed first (alphabetically), followed by all other LiquidO Consortium members (alphabetically). The primary authors were fully involved in the conception and execution of this study, including performing calculations, interpretation of results, evaluation of the scientific and technical considerations, development of the discussion and formulation of conclusions, and writing the paper. Consortium members were variously involved in developing LiquidO as a new idea and detection technique, including software for simulations. All authors reviewed and approved the submitted manuscript.

Competing interests

The authors declare no competing interests.

Additional information

Supplementary information The online version contains supplementary material available at https://doi.org/10.1038/s42005-026-02518-6.

Correspondence and requests for materials should be addressed to A. Cabrera, M. Chen, F. Mantovani, A. Serafini or V. Strati.

Peer review information *Communications Physics* thanks Dave Wark and the other anonymous reviewer(s) for their contribution to the peer review of this work.

Reprints and permissions information is available at http://www.nature.com/reprints

Publisher's note Springer Nature remains neutral with regard to jurisdictional claims in published maps and institutional affiliations.

Open Access This article is licensed under a Creative Commons Attribution-NonCommercial-NoDerivatives 4.0 International License, which permits any non-commercial use, sharing, distribution and reproduction in any medium or format, as long as you give appropriate credit to the original author(s) and the source, provide a link to the Creative Commons licence, and indicate if you modified the licensed material. You do not have permission under this licence to share adapted material derived from this article or parts of it. The images or other third party material in this article are included in the article's Creative Commons licence, unless indicated otherwise in a credit line to the material. If material is not included in the article's Creative Commons licence and your intended use is not permitted by statutory regulation or exceeds the permitted use, you will need to obtain permission directly from the copyright holder. To view a copy of this licence, visit http://creativecommons.org/licenses/by-nc-nd/4.0/.

© The Author(s) 2026

LiquidO Collaboration

A. Cabrera[1,2,3] ✉, M. Chen[4] ✉, F. Mantovani[5,6] ✉, A. Serafini[5,6,7,8] ✉, V. Strati[5,6] ✉, J. Apilluelo[9], L. Asquith[10], J. L. Beney[11], T. J. C. Bezerra[10], M. Bongrand[11], C. Bourgeois[2], D. Breton[2], M. Briere[2], J. Busto[12], A. Cadiou[11], E. Calvo[13], V. Chaumat[2], E. Chauveau[14], B. J. Cattermole[10], P. Chimenti[15], C. Delafosse[2], H. de Kerret[3,24], S. Dusini[7], A. Earle[10], C. Frigerio-Martins[15], J. Galán[9], J. A. García[9], R. Gazzini[2], A. Gibson-Foster[10], A. Gallas[2], C. Girard-Carillo[16], W. C. Griffith[10], F. Haddad[11], J. Hartnell[10], A. Hourlier[17], G. Hull[2], I. G. Irastorza[9], L. Koch[16], P. Laniéce[2,18], J. F. Le Du[1,2], C. Lefebvre[4], F. Lefevre[11], F. Legrand[2], P. Loaiza[2], J. A. Lock[10], G. Luzón[9], J. Maalmi[2], C. Marquet[14], M. Martínez[9], B. Mathon[2], L. Ménard[2,18], D. Navas-Nicolás[2], H. Nunokawa[19], J. P. Ochoa-Ricoux[20], M. Obolensky[3], C. Palomares[13], P. Pillot[11], J. C. C. Porter[10], M. S. Pravikoff[14], H. Ramarijaona[2], M. Roche[14], P. Rosier[2], B. Roskovec[21], M. L. Sarsa[9], W. Shorrock[10], L. Simard[2], H. Th. J. Steiger[16,22], D. Stocco[11], J. S. Stutzmann[11], F. Suekane[3,23], A. Tunc[16], M. -A. Verdier[2,18], A. Verdugo[13], B. Viaud[11], S. M. Wakely[16] & F. Yermia[11]

[1]LNCA Underground Laboratory, CNRS, EDF, Chooz Nuclear Reactor, Chooz, France. [2]IJCLab, CNRS/IN2P3, Université Paris-Saclay, Orsay, France. [3]APC, CNRS, Université de Paris Cité, Paris, France. [4]Department of Physics, Engineering Physics & Astronomy, Queen's University, Kingston, ON, Canada. [5]INFN, Sezione di Ferrara, Ferrara, Italy. [6]Dipartimento di Fisica e Scienze della Terra, Università di Ferrara, Ferrara, Italy. [7]INFN, Sezione di Padova, Padova, Italy. [8]Dipartimento di Fisica e Astronomia, Università di Padova, Padova, Italy. [9]Centro de Astropartículas y Física de Altas Energías (CAPA), Universidad de Zaragoza, Zaragoza, Spain. [10]Department of Physics and Astronomy, University of Sussex, Brighton, UK. [11]Subatech, IMT-Atlantique, CNRS, Nantes Université, Nantes, France. [12]CPPM, CNRS, Université de Aix Marseille, Marseille, France. [13]CIEMAT, Centro de Investigaciones Energéticas Medioambientales y Tecnológicas, Madrid, Spain. [14]LP2I, CNRS, Université de Bordeaux, Bordeaux, Gradignan, France. [15]Departamento de Física, Universidade Estadual de Londrina, Londrina, Brazil. [16]Institut für Physik, Johannes Gutenberg-Universität Mainz, Mainz, Germany. [17]IPHC, CNRS, Université de Strasbourg, Strasbourg, France. [18]IJCLab, Université Paris Cité, Orsay, France. [19]Department of Physics, Pontifícia Universidade Católica do Rio de Janeiro, Rio de Janeiro, Brazil. [20]Department of Physics and Astronomy, University of California at Irvine, Irvine, CA, USA. [21]Institute of Particle and Nuclear Physics, Charles University, Prague, Czechia. [22]Detektorlabor, Exzellenzcluster PRISMA+, Johannes Gutenberg-Universität Mainz, Mainz, Germany. [23]RCNS, Tohoku University, Sendai, Japan. [24]Deceased: H. de Kerret.